Supplementary material not submitted to the journal

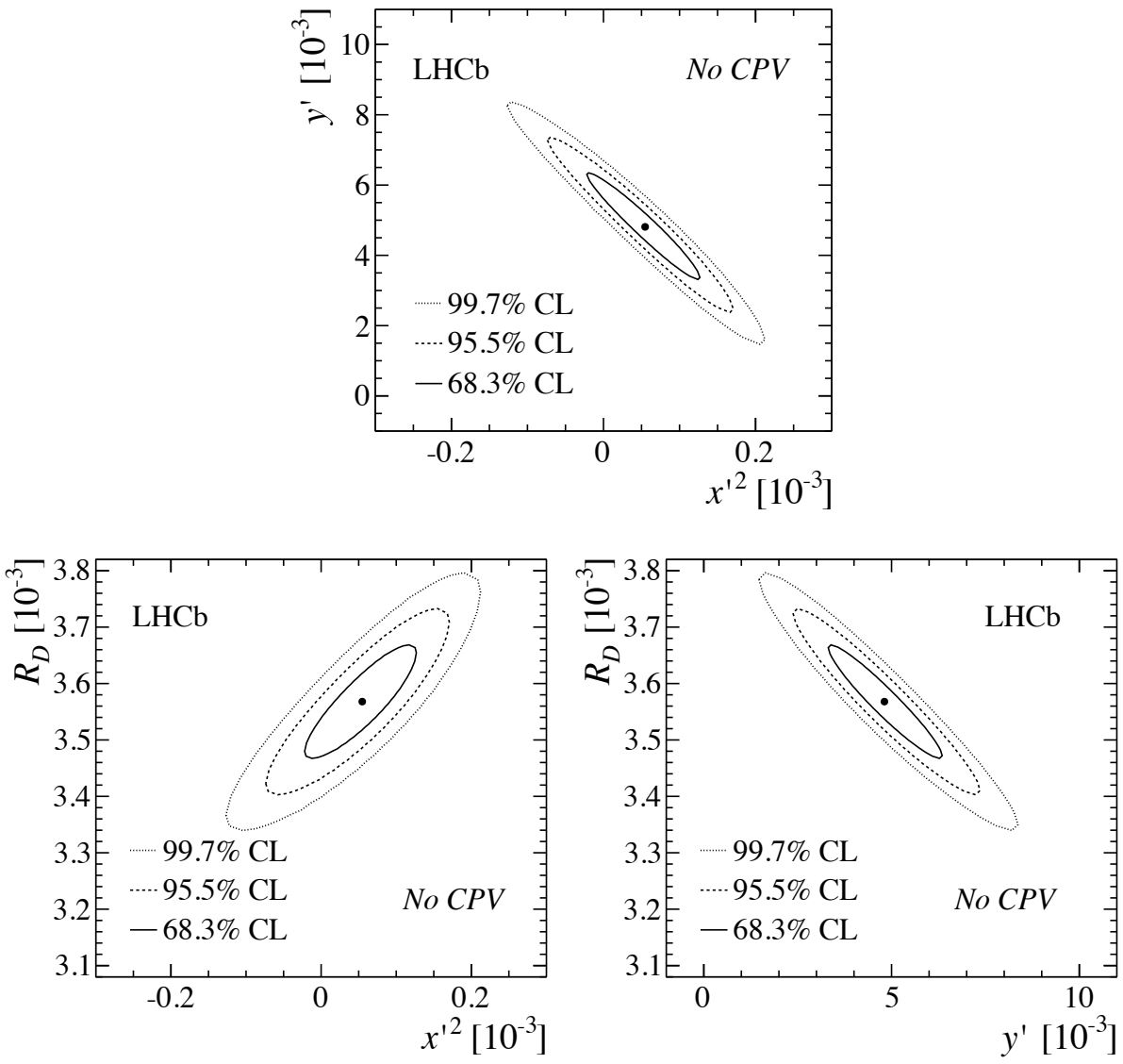

Figure 4: Confidence regions in the (top) (x'^2, y'), (bottom left) (x'^2, R_D), and (bottom right) (y', R_D) planes as obtained by the fit with no *CP* violation. Systematic uncertainties are included.

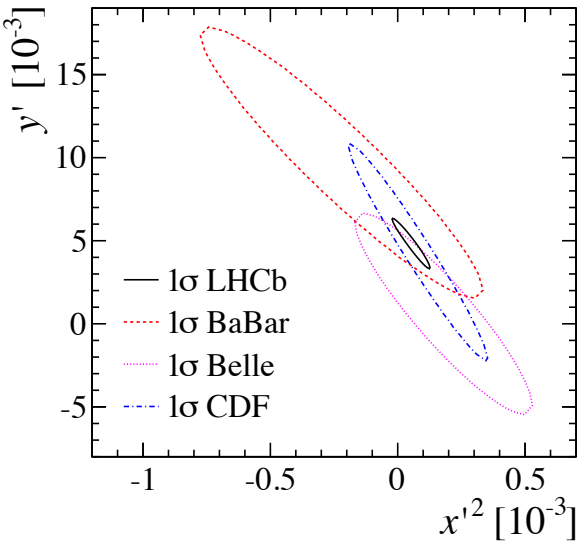

Figure 5: Comparison of the 68.3% CL regions in the (x'^2, y') plane between the present result and recent results from the BaBar [Phys. Rev. Lett. **98**, 211802 (2007)], Belle [Phys. Rev. Lett. **96**, 151801 (2006)], and CDF [`arXiv:1309.4078` (2013)] experiments.

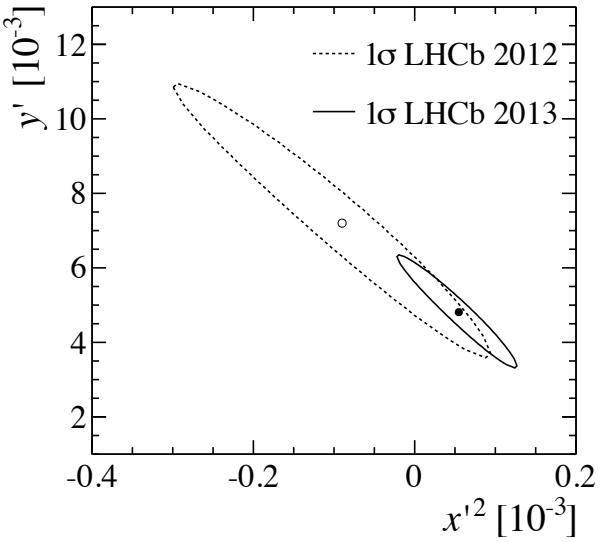

Figure 6: Comparison of the 68.3% CL regions in the (x'^2, y') plane between the present result (LHCb 2013) and the previous result based on a subset of the present data (LHCb 2012 [Phys. Rev. Lett. **110**, 101802 (2013)]). The points represent the best-fit values.

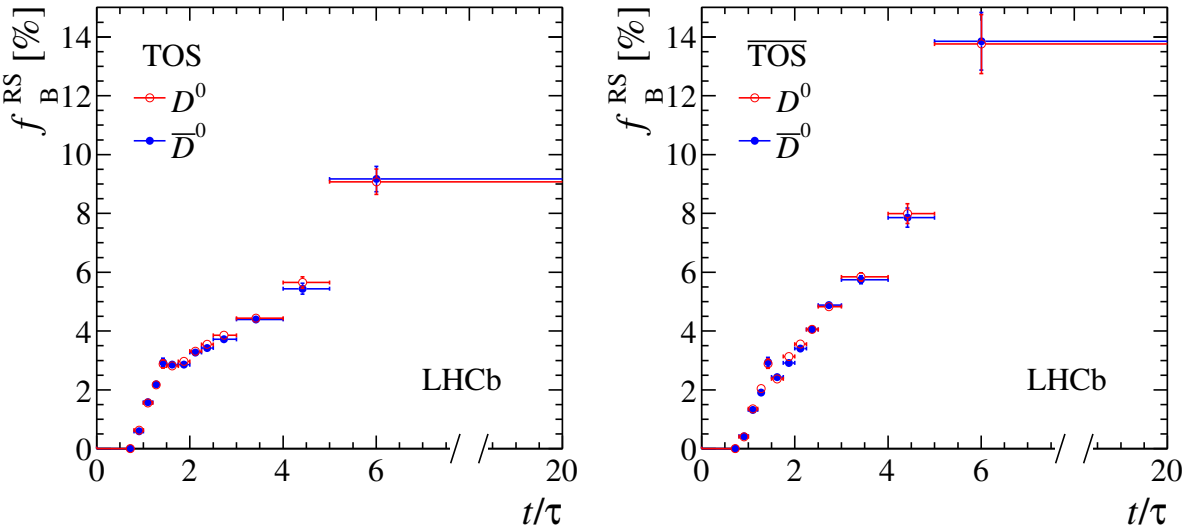

Figure 7: Decay-time evolution of the contamination from secondary D decays in the RS sample for (left) TOS and (right) $\overline{\text{TOS}}$ trigger categories, separately for D^0 and $\overline{D}^0$ decays. The uncertainties are correlated between D^0 and $\overline{D}^0$ decays.

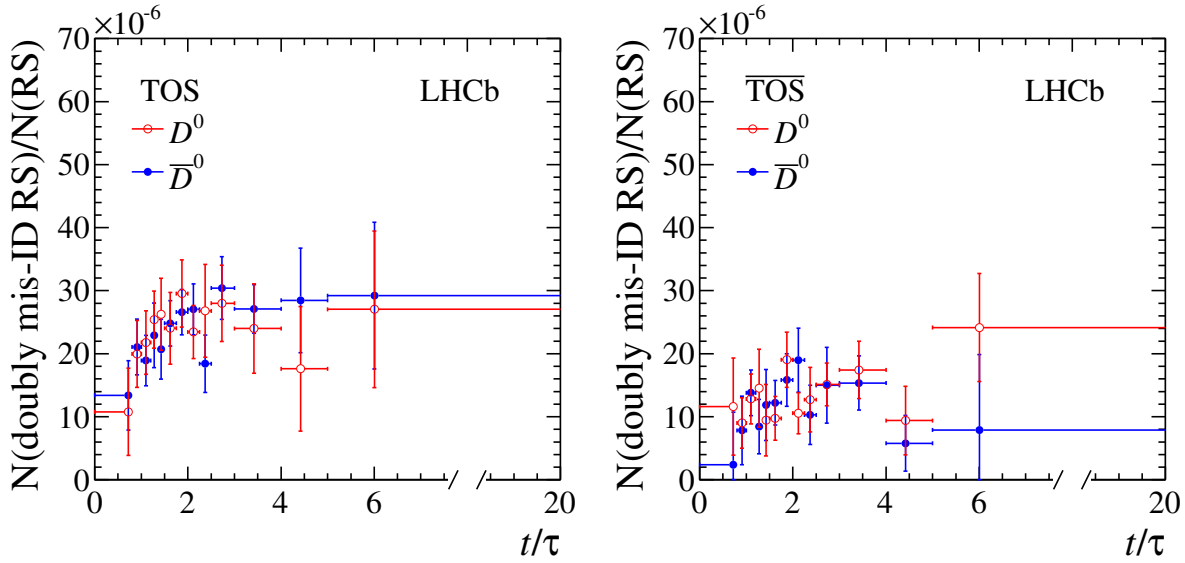

Figure 8: Decay-time evolution of the contamination from doubly misidentified RS candidates normalized to the RS signal yield for (left) TOS and (right) $\overline{\text{TOS}}$ trigger categories, separately for D^0 and $\overline{D}^0$ decays. The particle identification performances affect differently the TOS and $\overline{\text{TOS}}$ samples as they have different momentum distributions.

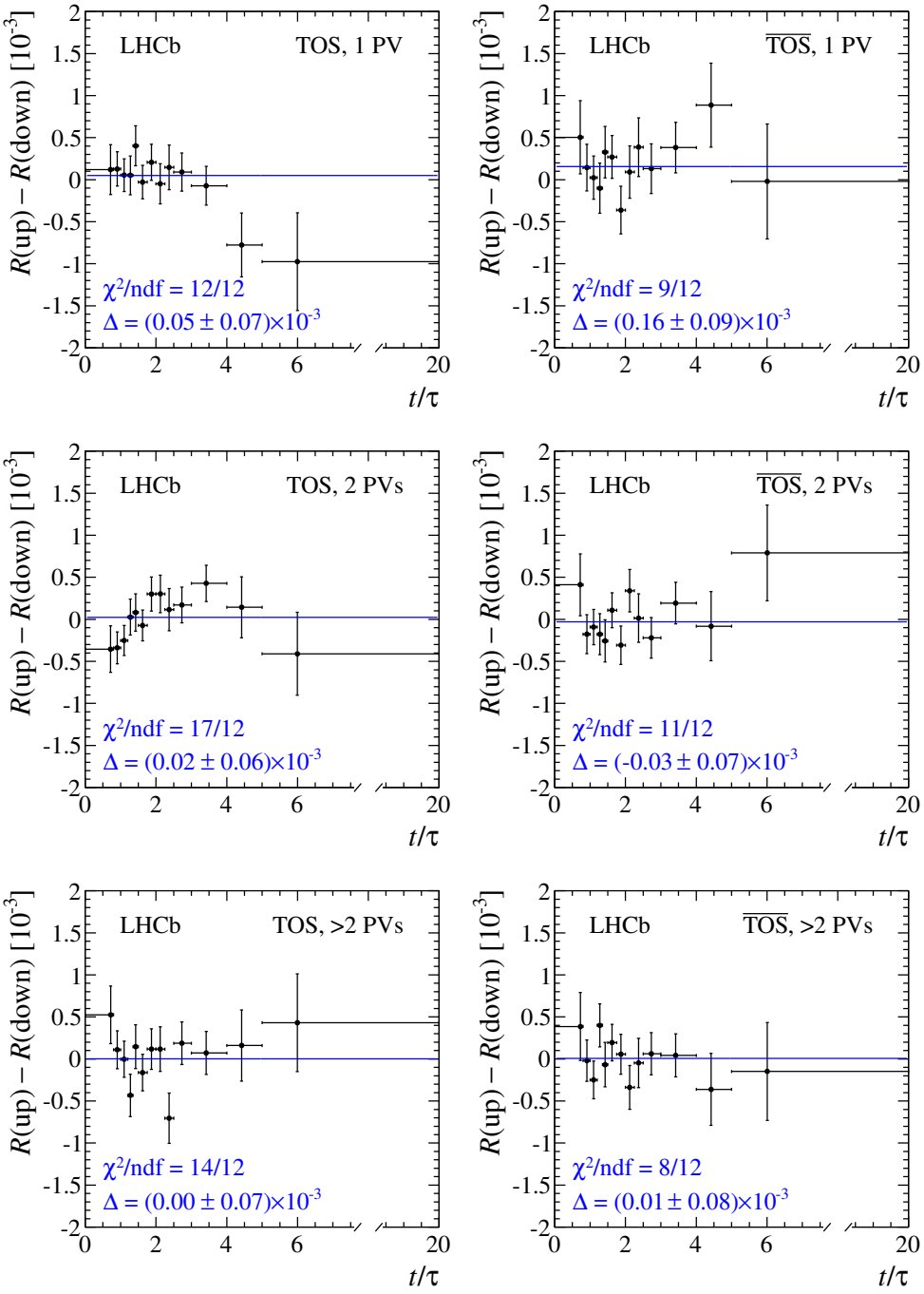

Figure 9: Decay-time evolution of the difference between WS-to-RS ratios observed in data collected with opposite magnet polarities, for different number of primary vertices (from top to bottom) and separately for (left) TOS and (right) $\overline{\text{TOS}}$ trigger categories, with projections of a fit to a constant overlaid. The fit value and χ^2 are also shown.

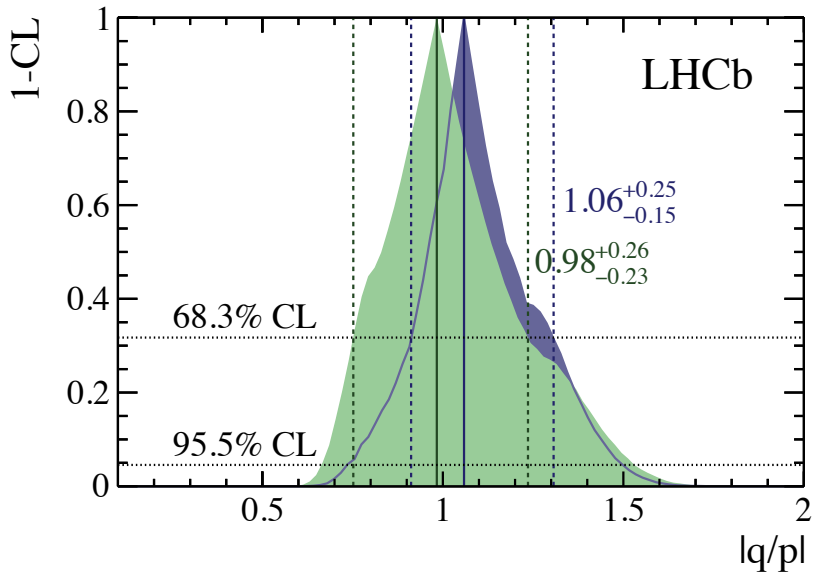

Figure 10: Graphs showing $1 - \mathrm{CL}$ as a function of $|q/p|$ for the (green) direct and indirect *CP* violation and (blue) indirect-only *CP* violation fit results. The reported numbers correspond to the best-fit value and the uncertainties are computed using the respective 68.3% CL intervals. The intervals at the 68.3% and 95.5% CL when direct and indirect (indirect only) *CP* violation is allowed are $0.75 < |q/p| < 1.24$ ($0.91 < |q/p| < 1.31$) and $0.67 < |q/p| < 1.52$ ($0.74 < |q/p| < 1.49$), respectively.

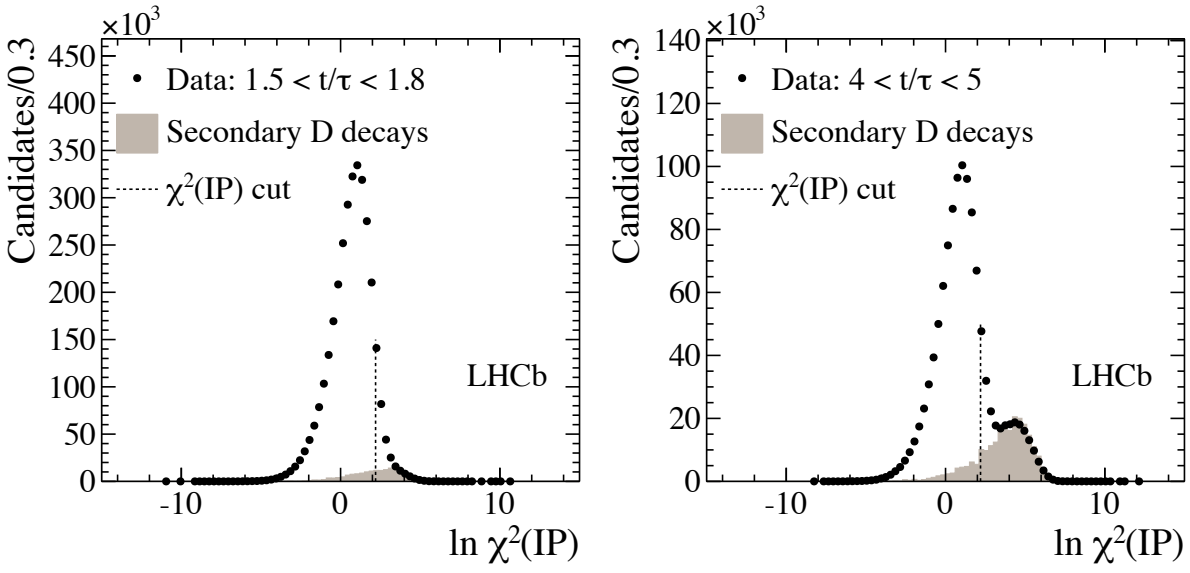

Figure 11: Background-subtracted distributions of impact parameter χ^2 for RS decays in two different decay-time bins. The dashed line indicates the analysis selection requirement; the shaded histogram represents the estimated secondary component.

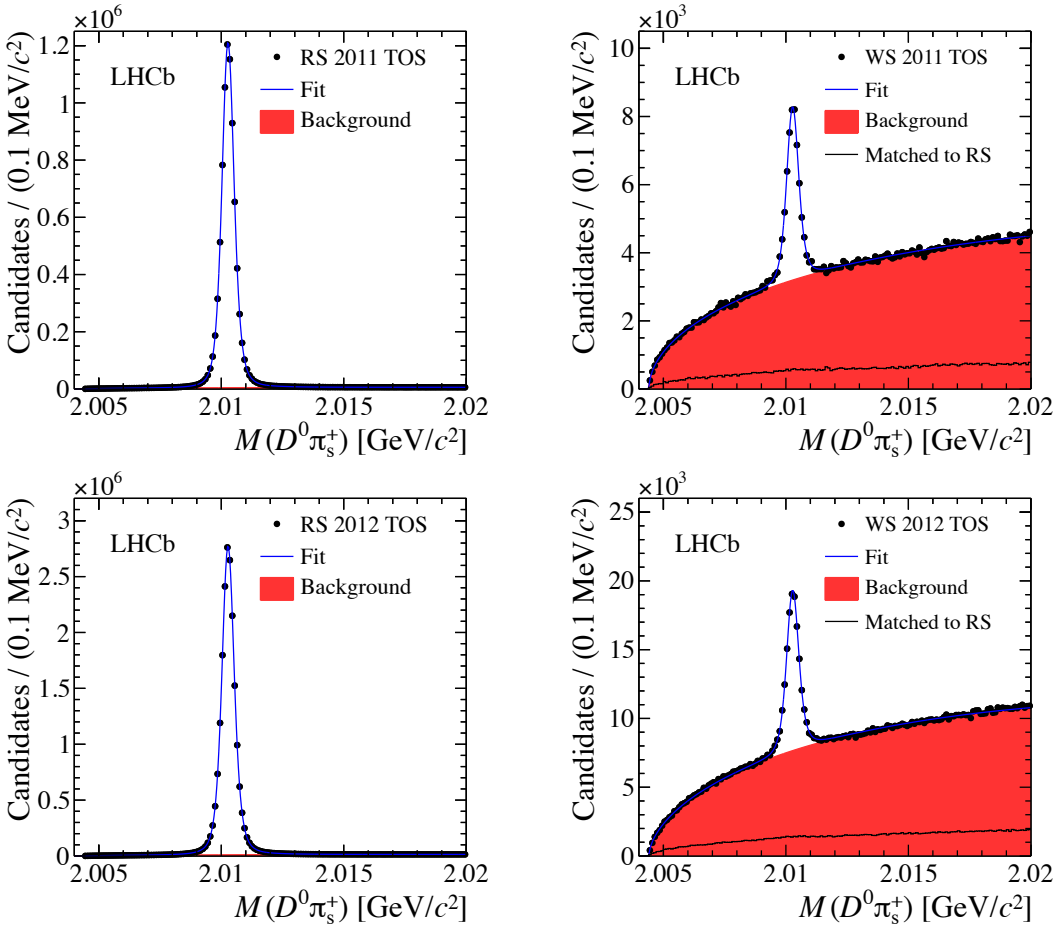

Figure 12: Distribution of $M(D^0\pi_s^+)$ for (left) RS and (right) WS TOS candidates from (top) 2011 and (bottom) 2012 data. The solid black histograms in the right panels show the distribution of candidates that are removed because their D^0 candidate is consistent with forming also a RS candidate with $M(D^0\pi_s^+)$ within 3 MeV/c^2 of the known D^{*+} mass.

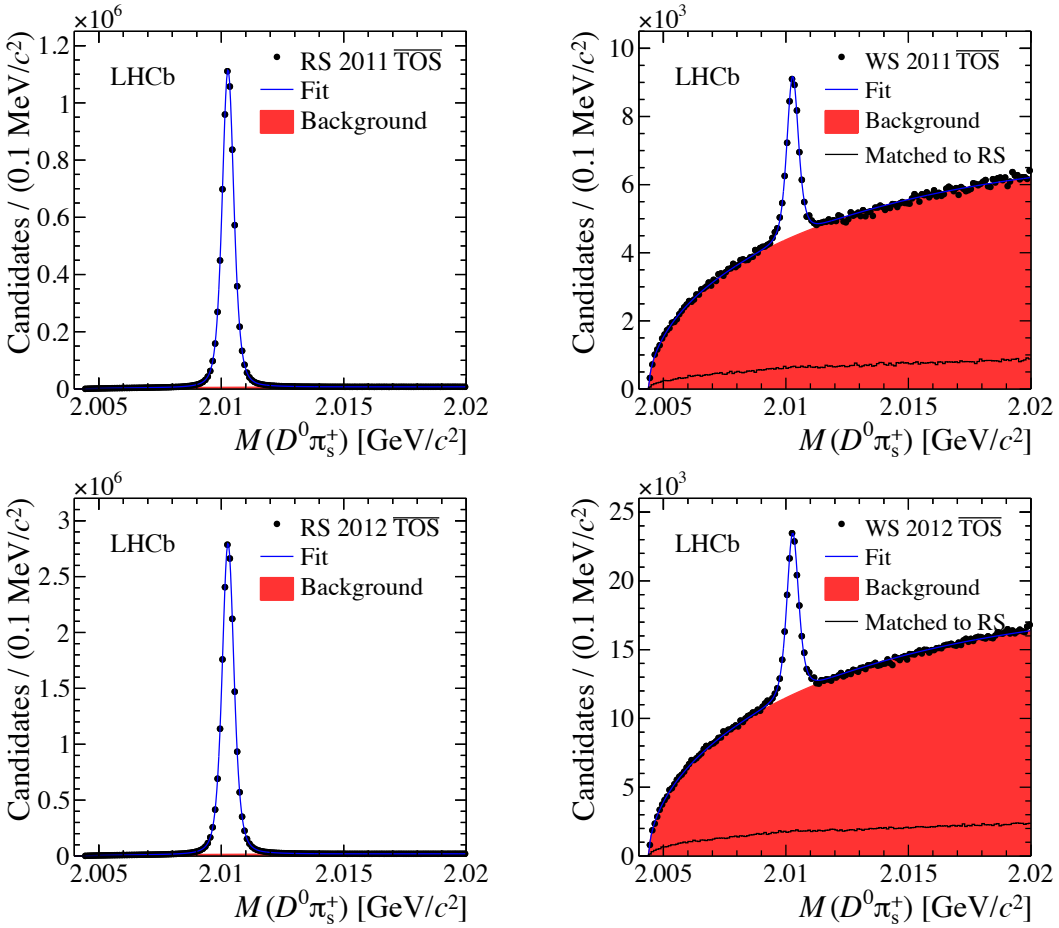

Figure 13: Distribution of $M(D^0\pi_s^+)$ for (left) RS and (right) WS $\overline{\text{TOS}}$ candidates from (top) 2011 and (bottom) 2012 (bottom) data. The solid black histograms in the right panels show the distribution of candidates that are removed because their D^0 candidate is consistent with forming also a RS candidate with $M(D^0\pi_s^+)$ within 3 MeV/c^2 of the known D^{*+} mass.

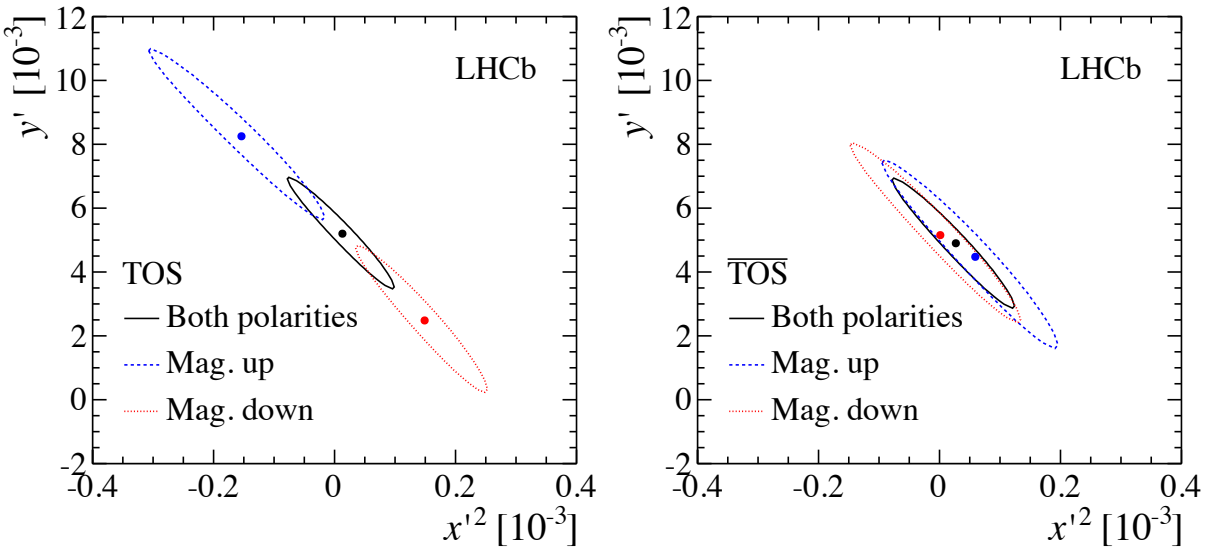

Figure 14: Comparison of 68% CL (x'^2, y') regions and best fit-values as derived from the samples corresponding to different magnet polarities (both polarities in black, up polarity in blue, down polarity in red) and different trigger categories (left is TOS, right is $\overline{\text{TOS}}$). Systematic uncertainties are not included.